Physical Properties of Polymorphic Yeast Prion Amyloid Fibers

Carlos E. Castro,[†‡] Jijun Dong,[§] Mary C. Boyce,[†] Susan Lindquist,[§¶] and Matthew J. Lang[†‖]*

[†]Department of Mechanical Engineering, Massachusetts Institute of Technology, Cambridge, Massachusetts; [‡]Department of Mechanical and Aerospace Engineering, The Ohio State University, Columbus, Ohio; [§]Whitehead Institute for Biomedical Research, Cambridge, Massachusetts; [¶]Howard Hughes Medical Institute and Department of Biology, Massachusetts Institute of Technology, Cambridge, Massachusetts; and [‖]Department of Chemical and Biomolecular Engineering, Vanderbilt University, Nashville, Tennessee

ABSTRACT   Amyloid fibers play important roles in many human diseases and natural biological processes and have immense potential as novel nanomaterials. We explore the physical properties of polymorphic amyloid fibers formed by yeast prion protein Sup35. Amyloid fibers that conferred distinct prion phenotypes ([PSI⁺]), strong (S) versus weak (W) nonsense suppression, displayed different physical properties. Both S[PSI⁺] and W[PSI⁺] fibers contained structural inhomogeneities, specifically local regions of static curvature in S[PSI⁺] fibers and kinks and self-cross-linking in W[PSI⁺] fibers. Force-extension experiments with optical tweezers revealed persistence lengths of 1.5 μm and 3.3 μm and axial stiffness of 5600 pN and 9100 pN for S[PSI⁺] and W[PSI⁺] fibers, respectively. Thermal fluctuation analysis confirmed the twofold difference in persistence length between S[PSI⁺] and W[PSI⁺] fibers and revealed a torsional stiffness of kinks and cross-links of ~100–200 pN·nm/rad.

INTRODUCTION

Amyloid fibers are highly ordered, β-sheet-rich protein assemblies. Although amyloid fibers are associated with a range of human diseases (1), they also serve beneficial biological functions such as biofilm formation in bacteria, environmental adaptation in yeast, and long-term memory in aplysia (2–5). Such ordered assemblies, which are accessible to many proteins and synthetic peptides, exhibit extremely high thermal and chemical stabilities (6,7). Amyloid formation can be triggered and regulated by diverse factors, such as pH changes, the presence of metal ions, or other environmental stresses (8,9). Because of the easy and controllable assembly of amyloid fibers, they are increasingly recognized as novel nanomaterials (NM) for applications including scaffolds for cell growth (10), templates for conducting nanowire formation (11), and functionalized biosensors (12), as well as several others (13–15). Furthermore, a single protein, when assembled under different conditions, can form amyloid fibers with distinct underlying structures (16) (molecular polymorphisms), referred to as amyloid variants. These amyloid variants often show different impacts in diseases and biological functions that likely result from distinct underlying properties. Indeed, amyloid variants formed by the same protein can exhibit very different thermal and chemical stabilities (16), and distinct mechanical stability of amyloid variants has also been suggested by their different fragmentation characteristics in turbulent solutions (17). However, variation in physical properties among amyloid variants has not been characterized in detail.

Here, we explored the mechanical properties of amyloid fibers formed from an N-terminal fragment (18) of the yeast *Saccharomyces cerevisiae* protein Sup35. Structurally

distinct amyloid variants of NM can be triggered in vitro and assayed in vivo by examining the induced prion status, making it an ideal system to study the impact of fiber physical properties on their biological functions. Sup35 consists of three domains: the C-terminal domain (C, amino acids 254–685) containing the translation termination function; the middle domain (M, amino acids 124–253), a highly charged region that imparts solubility; and the N-terminal domain (N, amino acids 1–123), with 5.5 imperfect repeats rich in glutamine and asparagines that are highly susceptible to amyloidogenesis. Amyloid assembly of Sup35 causes ribosomes to read through stop codons, resulting in extended protein translation. This reduction in the fidelity of protein translation leads to novel yeast phenotypes that are inheritable and transmissible via self-templated amyloid assembly (2,3,19). The N and M domains (18) form amyloid fibers in vitro. Extensive prior research on Sup35 has provided several useful tools for its biochemical manipulation (2,3,16,17,19–21). Defined assembly conditions, for example, different assembly temperatures, give rise to amyloid variants with distinct underlying prion structures (16,17). When these variants are introduced into prion-minus cells ([*psi*⁻]), they give rise to different degrees of stop-codon read-through, yielding phenotypically distinct prion strains in vivo (strong [PSI⁺] versus weak [PSI⁺]) (16). Strong and weak refer to the degree of phenotypic change from the wild-type yeast, and the amyloid variants were accordingly referred to as strong [PSI⁺] (^S[PSI⁺]NM) and weak [PSI⁺] (^W[PSI⁺]NM) fibers, respectively. Different degrees of resistance to mechanical fragmentation of ^W[PSI⁺]NM and ^S[PSI⁺]NM fibers has been identified as one of the key factors distinguishing prion strains (17). ^W[PSI⁺]NM fibers are more resistant to fragmentation than ^S[PSI⁺]NM fibers, indicative of higher mechanical stability, hence generating seeds for amyloid formation less efficiently and leaving

more functional Sup35 in solution. Hence, the prion proteins are unique in that the same protein can form functionally distinct fibers by adopting different folded geometries, whereas biopolymers such as F-actin are made from a highly conserved population of monomers and functional diversity is conferred by accessory proteins leading to bundles, cross-links, and meshes.

To understand the physical basis of prion strain diversity and its relation to molecular polymorphism, and to guide the potential use of amyloid fibers as nanomaterials, we used combined force-fluorescence microscopy with optical tweezers to quantify the mechanical behavior and microstructure of NM fibers from two distinct prion strains with unique underlying folded geometries. Optical tweezers have been widely used to characterize the mechanics of biopolymers including DNA (22,23), RNA (24), and M13 bacteriophage (25). Our lab has combined optical tweezers with optimized single-molecule fluorescence capabilities (26,27), making it possible to measure structure-function relationships of biopolymers. Here, we quantify the bending stiffness, extensional stiffness, and microstructure of [S[PSI+]]NM and [W[PSI+]]NM fibers in solution from both optical-force stretching and shape-fluctuation analysis by fluorescence imaging.

METHODS

Protein purification and labeling

Wild-type NM or NM with a single cysteine mutation at amino acid position 184 were cloned in the pNOTAG expression constructs (with no exogenous N- or C-terminal purification tags or epitopes). Proteins were purified as described in Serio et al. (20). NM monomers with a single cysteine mutation were labeled with either fluorescent dye or biotin according to the manufacturer protocols. In short, NM cysteine mutants (100 μM) were incubated in 6 M GdnHCl with 2 mM Alexa Fluor 555 C2 maleimide (Alexa555) (Invitrogen, Carlsbad, CA) or 2 mM maleimide-PEO2-biotin (Thermo Fisher Scientific, Rockford, IL) overnight at 4°C and purified using desalting columns.

Fiber preparation

Fibers were reconstituted in vitro from purified NM monomers (50% labeled with Alexa 555 and 50% unlabeled) at 4°C or 37°C in 1× CRBB buffer (5 mM potassium phosphate, 150 mM NaCl, and 5 mM TCEP). Assembly was seeded at 4°C by crude lysates of yeast cells with a strong [PSI+] phenotype and at 37°C by crude lysates of yeast cells with a weak [PSI+] phenotype.

Force-extension experiments with fluorescent imaging

A tethered fiber assay was developed as described in Dong et al. (28). Experiments were carried out in a fluid channel made of a glass coverslip attached to a microscope slide with two pieces of double-sided sticky tape to create a channel of ~10–15 μl in volume. His-tagged NM monomers were flowed into the channel at 0.5 μM and incubated for 15 min to allow for nonspecific adsorbtion to the glass coverslip surface. Then, 5 mg/ml casein (Sigma-Aldrich, St. Louis, MO) was flowed into the channel and incubated for

~40 min to cover the remaining surface and prevent subsequent nonspecific binding. Preformed fibers with 50% fluorescently labeled NM monomers were flowed into the chamber at a concentration of 0.5 μM and incubated for 30 min. When no NM monomers were deposited on the surface, we found less than one fiber per field of view (~15 × 15 μm) as opposed to around five fibers per field of view when NM monomers were present on the surface. Those fibers that did stick down in the negative control were generally not attached via a single point at one of the fiber ends and therefore would be ruled out of the pulling experiments upon initial imaging of the structure. Streptavidin-coated polystyrene beads 800 nm in diameter (Spherotech, Lake Forest, IL) were coated with both biotinylated NM monomers and Alexa488 fluorescent markers (Invitrogen) by incubating 10 μl of prewashed beads at 1% w/v with 500 μl of 5 μM biotinylated NM and 0.2 μM Alexa488 for 40 min at room temperature, 22°C. NM-coated beads were washed, flowed into the channel, and incubated overnight to allow beads to attach to free fiber ends. Slides were washed with 200 μl of assembly buffer between incubation steps. After the final bead incubation, slides were washed with 400 μl of assembly buffer to remove unbound fibers and beads from the flow channel. This protocol resulted in fibers tethered to the coverslip surface at one end and to an 800-nm polystyrene bead at the other end.

Before each pulling experiment, the tethered fiber and bead were fluorescently imaged to confirm the single fiber assay and identify fiber microstructure. Beads were initially centered over the surface attachment point and subjected to position and force calibrations (29). Force-extension experiments were performed by holding the bead in a stationary optical trap and moving the coverslip attachment point with a piezoelectric stage. Four unloading and four loading curves were collected for each fiber, two in each axis, yielding eight force-extension curves. Fibers were fluorescently imaged during deformation to identify boundary conditions. Fluorescence and excitation lasers were cycled out of phase at 50 kHz with a 10% duty cycle lag time in between.

Fluorescence imaging of morphology

Preformed fibers at a concentration of ~10–100 nM were sandwiched between two 20 × 40-mm polyethyleneglycol (PEG (molecular weight 5000; Laysan Bio, Arab, AL))-coated coverslips, allowing them to freely fluctuate in solution without any surface attachments. A sample height of ~50–100 nm was achieved by using a small sample volume (~0.1 μl), effectively constraining the fiber fluctuations to a 2D imaging plane. Fibers were visualized with a Nikon TE2000 microscope using a 1.45 total internal reflection fluorescence objective with epifluorescence excitation (532 nm). Images were recorded on a back-thinned electron-multiplying CCD camera (ANDOR).

Fluorescence imaging of thermal fluctuations

Dynamic thermal fluctuations of the fiber shape were monitored using a similar assay with a series of 250–300 frames recorded at ~5 Hz. For the bending-mode analysis, the filament in each frame of the sequence was skeletonized and smoothed and a cubic spline was fit to the skeletonized fiber to calculate the tangent angle, ϕ, as a function of arc length, s. The data analysis of shape fluctuations is detailed in the SI text.

The torsional stiffness of the hinge domains was determined using identical sample geometry and image processing as described previously. The hinge angle was determined by manually fitting straight lines to the skeletonized fiber and then visually confirmed using the fluorescence image (see Fig. 5 c, inset). Fluctuations in hinge angle were related to the hinge torsional stiffness to determine the hinge torsional stiffness.

Analysis of thermal shape fluctuations

The persistence length was calculated from thermal shape fluctuations using the approach of Gittes et al. (30), which is described in detail in

the Supporting Material. In summary, the fiber shape was decomposed into bending modes by fitting the arc length, s, versus tangent angle, ϕ, waveform with a Fourier series for every frame of the image sequence. The bending energy, E_b^n, of each mode, n, can then be written as $E_b^n = 1/2\,\kappa_b(n\pi/L_C)^2(a_n - a_n^0)^2$, where κ_b is the bending stiffness, L_C is the contour length, and a_n are the Fourier coefficients (a_n^0 are the Fourier coefficients for the unstressed fiber). According to the theorem of equipartition of energy, each bending mode contributes an energy of $k_BT/2$. This yields Eq. 1:

$$\left\langle \left(a_n - a_n^0\right)^2 \right\rangle = \frac{k_BT}{\kappa_b}(k_w)^2, \tag{1}$$

where the wave number is $k_w = n\pi/L_C$. The variations in Fourier coefficients, $\langle(a_n - a_n^0)^2\rangle$, were computed for bending modes 1–9 throughout the image sequence. The modes that followed a linear trend with a slope of -2 on a log-log plot of $\langle(a_n - a_n^0)^2\rangle$ versus k_w were fit using Eq. 1 to determine κ_b. The persistence length, L_p, was calculated from the equation $L_p = \kappa_b/k_BT$ (Fig. S3 in the Supporting Material).

RESULTS

Force-extension behavior of NM amyloid fibers

We developed a tethered fiber assay to simultaneously image fiber structure and deformation while measuring force-extension curves by optical trapping (28). Fibers tethered between a glass coverslip and a 0.8-μm polystyrene bead, were subjected to force-extension experiments by holding the bead in a stationary laser trap while scanning the surface tether point using a piezoelectric stage. Details of the experimental assay and loading protocol can be seen in Fig. 1. An interlaced optical force and fluorescence (IOFF) method, developed in our lab, avoids trap-induced photobleaching to enable imaging of the fiber morphology throughout the force-extension experiment and to properly determine the boundary conditions (26). This proved to be crucial for our data analysis, as shown below. When IOFF is not used, fiber and bead fluorescence in the vicinity of the trap bleached very quickly (Fig. 2 a). With IOFF, the entire fiber and bead were easily visible throughout the complete experiment (Fig. 2 b).

Force-extension measurements were initially conducted on $^{\text{S[PSI+]}}$NM fibers (Movie S1). We used lysates of yeast cells carrying a strong prion element to seed the polymerization of soluble fluorescently labeled NM. Assembly was performed at 4°C, a condition that further favors the production of strong prion variants. To assay the prion nature of these fluorescently labeled fibrils, they were used to transform prion-minus cells into prion-plus cells. All transformed cells yielded uniform strong prion phenotypes. Thus, these fibrils are biologically homogenous and of certain relevance to the prion state.
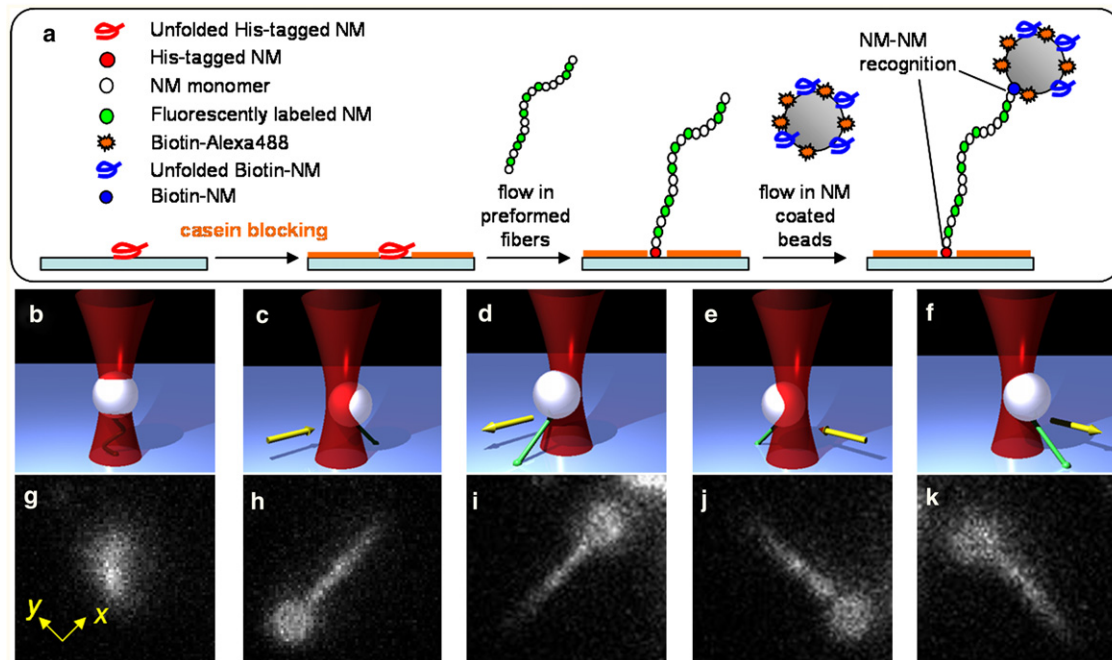

FIGURE 1 Schematics and fluorescent images of the experimental assay. (*a*) His-tagged NM monomers are nonspecifically adhered to a glass coverslip surface. The remaining exposed glass is coated with casein blocking protein to prevent preformed fibers and beads from nonspecifically sticking to the glass coverslip surface. Preformed NM fibers with 50% fluorescently labeled monomer are then flowed into the chamber and attached to the His-NM on the surface. Finally, fluorescently labeled streptavidin beads precoated with biotinylated NM monomers are flowed into the sample and attached to the free end of the fiber. Both the surface and bead attachment rely on the self-recognition properties of the NM protein. (*b–k*) The fiber is extended in the *x*-direction and the *y*-direction by displacing the piezoelectric sample stage as shown schematically (*b–f*) and from an experiment (*g–k*) resulting in eight force-extension curves for the fiber, four loading and four unloading.
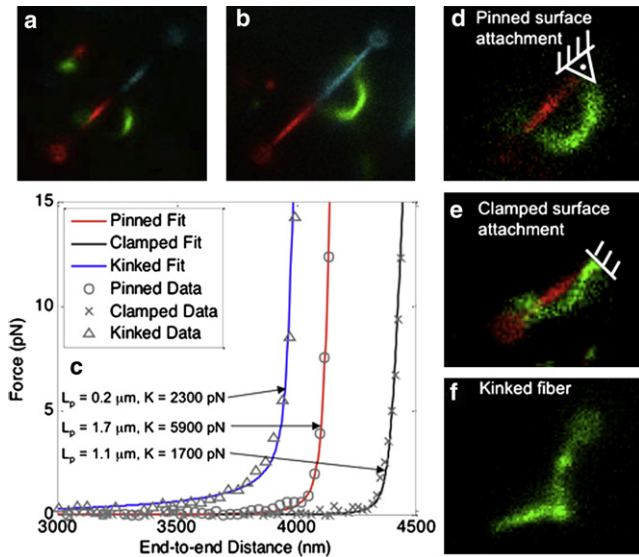
FIGURE 2 (a) Screen shots of fiber geometry throughout extension. The trapping laser excitation greatly accelerates photobleaching. (b) Cycling the trapping and fluorescence excitation lasers out of phase prolongs the fluorescence lifetime so that the entire fiber structure is visible through the experiment. (c) For fibers with a homogeneous structure, force-extension data were fit to a WLC model with appropriate boundary conditions to determine the persistence length, L_p, the contour length, L_C, and the axial extension modulus, K. (d and e) Boundary conditions were determined from the fluorescence images for a pinned (d) and a clamped (e) fiber. The force-extension data for kinked fibers (f) were fit to the microstructure-based model in Eq. 5. Achieving a similar fit for the kinked fiber with a WLC model (Eq. 4) results in an apparent persistence length of 0.2 μm. Beads are 800 nm in diameter.

Fitting of the force-extension curves to a wormlike chain (WLC) model allowed us to determine the contour length (25), persistent length (L_p), and axial stiffness (K) of the fibers. The force-extension curves (Fig. 2 c) are characteristic of an extensible WLC, with L_p comparable to L_C ($L_p \sim L_C$). Hence, we fit the force-extension curves with a WLC model consistent with $L_p \sim L_C$ (18), which accounts for the direct axial stretching that occurs as the end-to-end distance, r, approaches L_C (31). Our simultaneous force and fluorescence imaging revealed that some surface attachments were freely rotating (i.e., pinned (Fig. 2 d)), whereas some surface attachments were rigidly constrained against rotation (i.e., clamped (Fig. 2 e)). The clamped case likely occurs when some area in the vicinity of the surface-bound monomers remains unblocked by the casein, allowing more than one monomer to attach to the surface and inhibiting free rotation of the surface attachment. Any rotation resistance at the boundaries (i.e., attachment points) constrains the lateral motion of the fiber over a distance $\sim L_p$. Therefore, when $L_p \sim L_C$, as is the case for amyloid fibers, the boundary conditions become significant. The force-extension behavior of pinned amyloid fibers is described by Eqs. 2–4, whereas that of clamped amyloid fibers follows Eqs. 2a–4 (31).

$$F = \frac{k_b T}{L_p}\left(\frac{1}{4(1 - \lambda_u r_0/L_C)^2}\right)\left(\frac{L_C/L_p - 6(1 - \lambda_u r_0/L_C)}{L_C/L_p - 2(1 - \lambda_u r_0/L_C)}\right) \tag{2}$$

$$F = \frac{k_b T}{L_p}\left(\frac{1}{16(1 - \lambda_u r_0/L_C)^2}\right)\left(\frac{L_C/L_p - 24(1 - \lambda_u r_0/L_C)}{L_C/L_p - 8(1 - \lambda_u r_0/L_C)}\right) \tag{2a}$$

$$\lambda_e = \frac{L_C}{r_0}\frac{F}{K} + 1 \tag{3}$$

$$\lambda = \lambda_e \lambda_u = r/r_0. \tag{4}$$

In these equations, F is the force acting on the fiber; λ is the total fiber stretch, which is decomposed into λ_u, the stretch due to the reduction in thermal fluctuations of the fiber due to F, and λ_e, the stretch due to direct axial extension; r is the current end-to-end distance; and r_0 is the initial end-to-end distance, which is derived from Eq. 2 as $r_0 = L_C(1 - L_C/6L_p)$ (or $r_0 = L_C(1 - L_C/24L_p)$ for the clamped case).

In addition to specifying boundary conditions (i.e., pinned or clamped), our combined force-fluorescence approach revealed that some fibers contained kinks (see Fig. 2 f and Movie S2). Their force-extension behavior was similar to a homogeneous long polymer ($L_C \gg L_p$). To provide a means for direct comparison to the homogeneous fibers, we momentarily ignored the kinked microstructure and fit the force-extension data to the Marko-Siggia WLC model (22,32) given in Eq. 5, which assumes $L_C \gg L_p$, to determine L_C, an apparent L_p, and K.

$$F = \frac{k_b T}{L_p}\left(\frac{1}{4(1 - r/L_C + F/K)^2} - \frac{1}{4} - \frac{F}{K}\right). \tag{5}$$

Representative results of fitting the pinned, clamped, and kinked fibers to WLC models are shown in Fig. 2 c. Fitting the clamped data in Fig. 2 c with pinned boundary conditions results in overpredicting L_p by a factor of 3, thus demonstrating the importance of visually identifying and accounting for the fiber boundary conditions. Fig. 3 a shows the distributions of L_p for homogeneous [S[PSI+]]NM fibers, which are broken up into pinned (blue) and clamped (red) boundary conditions, and the apparent L_p of the kinked fibers (gray). The L_p of the homogeneous fibers was 1.5 ± 0.6 μm (mean ± SD), which corresponds to a bending stiffness (κ_b) of 0.6 × 10^{-26} ± 0.2 × 10^{-26} N·m^2. The structural inhomogeneities that give rise to kinks result in a significantly reduced apparent L_p of 0.3 ± 0.1 μm. However, as shown in Fig. 3 b, kinks do not affect axial stiffness (K) (5600 ± 2800 pN and 4000 ± 2400 pN for the homogenous and kinked fibers, respectively).

A model for the force-extension behavior of the kinked fibers that specifically accounts for the kinked morphology
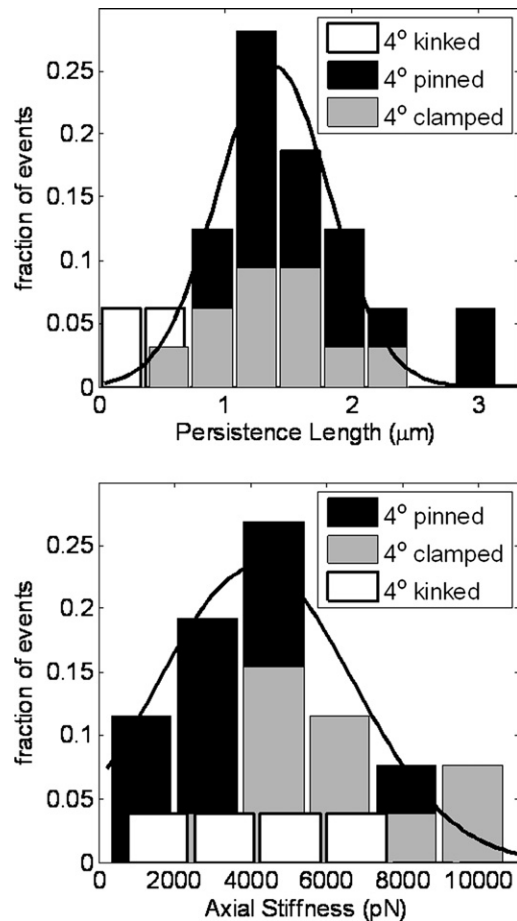
FIGURE 3 The persistence length and the stretching modulus were determined from force-extension experiments on single fibers. The average persistence length is 1.5 μm, which corresponds to a bending stiffness of 0.6×10^{-26} N·m^2, and an average axial stiffness of 5600 pN. Imaging revealed local inhomogeneities in fiber structure resulting in some kinked fibers. These fibers have a low apparent persistence length compared to the homogenous fibers, but the axial stiffness is similar.

was developed (see Section 1 of the Supporting Material for derivation). The model considers two stiff rods connected by a flexible hinge with equilibrium angle θ_0 and torsional stiffness κ_θ. The thermal fluctuations of the hinge were not included, because the change in internal energy dominates over configurational entropy changes since $\kappa_\theta \theta^*$ is $>> k_B T$, where θ^* is a characteristic angular deformation that is ≈ 1 (determined from fluorescence images). The force-extension of the kinked structure including axial extension is given by Eq. 6,

$$F = \frac{\kappa_\theta(r_{tot} - FL_C/K)}{L_1 L_2 (1 - \cos^2 \theta)^{1/2}} (\theta - \theta_0), \qquad (6)$$

where $\theta = \arccos(L_1^2 + L_2^2 - (r_{tot} - FL_C/K)^2/2L_1L_2)$, and L_1 and L_2 are the lengths of the fibers connected by the hinge. The force-extension data of the kinked fiber shown in Fig. 2 c were fit to Eq. 6, where the parameters $L_1 = 1.55$ μm,

$L_2 = 1.01$ μm, and the initial kink angle $\theta_0 = 109°$, were determined from fluorescence images. This fit resulted in κ_θ of 5.5×10^{-19} N·m/rad and $K = 1800$ pN. With no prior knowledge of a kink, achieving similar fits using a WLC model leads to an apparent L_p of 0.3 μm as shown above, thus demonstrating the importance of identifying microstructure in determining accurate fiber mechanical properties.

We then characterized $^{W[PSI+]}$NM fibers, which are assembled by using lysates of yeast cells carrying a weak prion element, as seeds. Assembly was performed at 37°C, a condition that further favors the production of weak prion variants. When prion-minus cells were transformed with these fluorescently labeled fibrils, transformants yielded uniform weak prion phenotype. Compared to $^{S[PSI+]}$NM fibers, $^{W[PSI+]}$NM fibers frequently led to complex kinked and cross-linked morphologies. Furthermore, through an unknown mechanism, beads stuck to the sides of $^{W[PSI+]}$NM fibers more often than to $^{S[PSI+]}$NM fibers (see Fig. S2). Despite these difficulties, five reliable force-extension traces were obtained for $^{W[PSI+]}$NM fibers. These fits resulted in an average L_p of 3.3 $\pm$ 1.5 μm and an average axial stiffness of 9100 $\pm$ 6600 pN. Since force-extension experiments proved to be an inefficient means of characterizing $^{W[PSI+]}$NM fibers, we chose to also characterize the persistence lengths of both $^{W[PSI+]}$NM and $^{S[PSI+]}$NM by an analysis of thermal shape fluctuations to effectively compare the prion variants.

NM amyloid fiber equilibrium morphologies

To our surprise, NM fibers produced from a self-templated assembly that yielded biologically homogeneous phenotypes exhibited complex and inhomogeneous morphologies. Therefore, the microstructure of NM fibers was further characterized by fluorescence imaging of isolated fibers in solution. A volume of ~0.1 μl of the preformed fluorescently labeled NM fibers was sandwiched between two PEG-coated coverslips, preventing fiber attachment to the surface. This resulted in a sample height of 50–100 nm, allowing for tracking of fibers freely fluctuating in a 2D image plane (Movie S3). The lengths of individual fibers varied from ~1 μm to ~20 μm, and quantitative measurements and analysis focused on fibers with L_C ranging from 3 μm to 10 μm.

Fluorescence images revealed complex morphologies in the equilibrium structures of both $^{S[PSI+]}$NM and $^{W[PSI+]}$NM fibers. The equilibrium morphologies of $^{S[PSI+]}$NM fibers varied from apparently homogeneous straight fibers (Fig. 4, a–c), to fibers with local regions of static curvature with radii of curvature varying from ~0.1 μm to ~5 μm (Fig. 4, d and e). Some fibers exhibited point inhomogeneities resulting in static kinks (Fig. 4, e and f). Of the $^{S[PSI+]}$NM fibers (75 total), 53% had apparently straight homogeneous morphologies, whereas 41% contained regions of static curvature and 8%
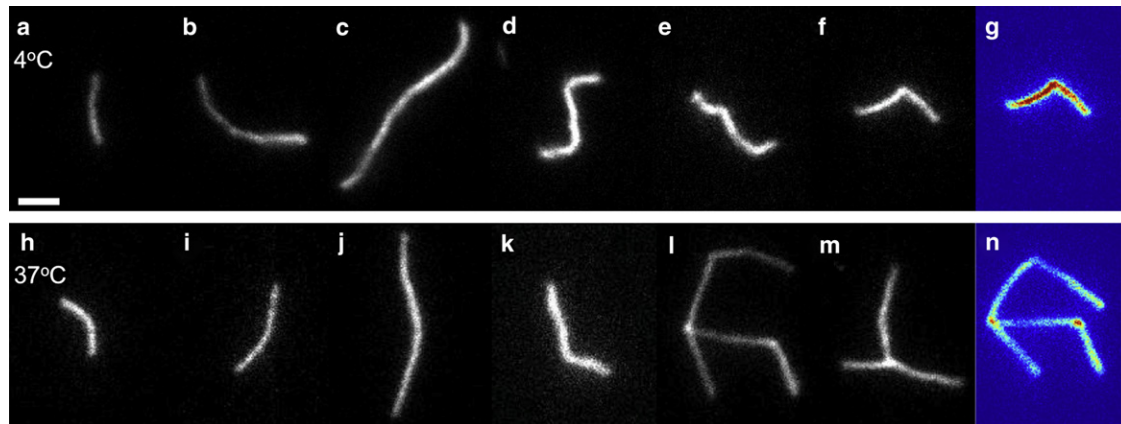
FIGURE 4 Fluorescently labeled NM fibers reconstituted in vitro exhibit complex physical properties shown by snapshots of the morphology of several fibers fluctuating in solution, at 4°C (*a–g*) and 37°C (*h–n*) (scale bar, 2 μm). $^{S[PSI+]}$NM fibers show different degrees of bending due to thermal fluctuations (*a–c*), and some fibers have a stress-free configuration containing regions of high curvature (*d* and *e*) or local sharp turns (kinks) in the fiber (*e* and *f*). The $^{S[PSI+]}$NM kinks do not contain overlapping NM monomers, as indicated by the smoothly varying intensity contour (*g*). $^{W[PSI+]}$NM fibers exhibit some similar homogeneous (*h–j*), bent (*k*), and kinked (*l*) structures in solution. Some $^{W[PSI+]}$NM fibers form branching cross-links (*l* and *m*). Both the cross-links and some of the kinks seem to contain additional NM monomers, as indicated by the higher intensity at junction points (*n*).

contained single kinks. Two fibers contained both a kink and static curvature, as in Fig. 4 *e*.

The $^{W[PSI+]}$NM fibers (53 total) exhibited a similar percentage of homogeneous fibers (Fig. 4, *h–j*)), 51%; however, only 15% of the fibers contained regions of static curvature (Fig. 4 *k*), and 34% contained either branching cross-links (Fig. 4, *l* and *m*)) or kinks (Fig. 4 *m*). Closer inspection of the kinks in the $^{W[PSI+]}$NM fibers showed that many differed in nature from those in $^{S[PSI+]}$NM fibers . As seen in the intensity contour plot of the kinked $^{S[PSI+]}$NM fiber in Fig. 4 *g*, the fluorescence varies smoothly along the fiber, suggesting that the kink is not a result of overlapped NM monomers. The fluorescence intensity contour plot of the $^{W[PSI+]}$NM fiber in Fig. 4 *n* reveals a similar kink (at the top) and two kinks that emit higher fluorescence intensity, suggesting an overlap of NM monomers. The overlapping kink on the left forms a branching cross-link between two (possibly three) fibers. Approximately 80% of the kinks in $^{W[PSI+]}$NM fibers contained overlapping monomers compared to none in the $^{S[PSI+]}$NM fibers. Of that 80%, three quarters formed branching cross-links between fibers as in Fig. 4 *l* and the left kink of Fig. 4 *n*.

Fluctuation imaging to measure persistence length and hinge torsional stiffness

Since the force-extension measurements could not provide a thorough characterization of the $^{W[PSI+]}$NM fibers, we sought to compare the mechanical behavior of the NM amyloid variants with a fluorescent-imaging-based shape-fluctuation analysis. As described in the previous section, we constrained fibers in a 2D imaging plane to track their fluctuation free in solution. The magnitude of fiber shape fluctuations can be directly correlated to fiber bending

stiffness or persistence length (30,33) through bending-mode or cosine-correlation analysis. A sequence of at least 200 frames of thermally fluctuating fluorescent fibers were imaged and skeletonized to determine fiber shape (Fig. 5 *a*). A bending-mode analysis (30) was used to determine the persistence length by reducing the fiber shape into a Fourier series and estimating the bending stiffness from the variation in amplitude of the Fourier mode coefficients (Fig. 5 *b*). Cosine-correlation methods, which determine persistence length by tangent-angle correlations (33), were inappropriate in this case, because the inherent equilibrium curvature of some of the fibers, as we previously observed (Fig. 4), would yield an apparently lower L_p. From the bending-mode analyses (21 fibers for each case), the persistence lengths were found to be 3.6 ± 1.1 μm and 7.0 ± 2.4 μm (mean ± SD) for the $^{S[PSI+]}$NM and $^{W[PSI+]}$NM fibers, respectively. The results are shown in Fig. 5 *b*. Fibers with static curvature and apparently straight fibers were indistinguishable in terms of L_p. Kinked fibers were omitted from any bending-mode analysis.

There is a 2- to 2.5-fold difference in L_p measured by thermal fluctuations versus L_p from force-extension. Such a difference between active and passive measurements was consistently reported for actin filaments and insulin fibers (33–35). In the force-extension experiments, high forces are applied via specific attachments to the filaments. Thus, nonlinearities in the mechanical response might play a role in active measurements, giving rise to different results from passive measurements (36).

Torsional stiffness of the kinks was determined by measuring the thermal fluctuations in the kink angle, θ (35,36), using a similar assay (Movie S4). The kink angle was fit manually over a series of skeletonized images by selecting three points to define θ (Fig. 5 *c*). Fig. 5 *d* shows the
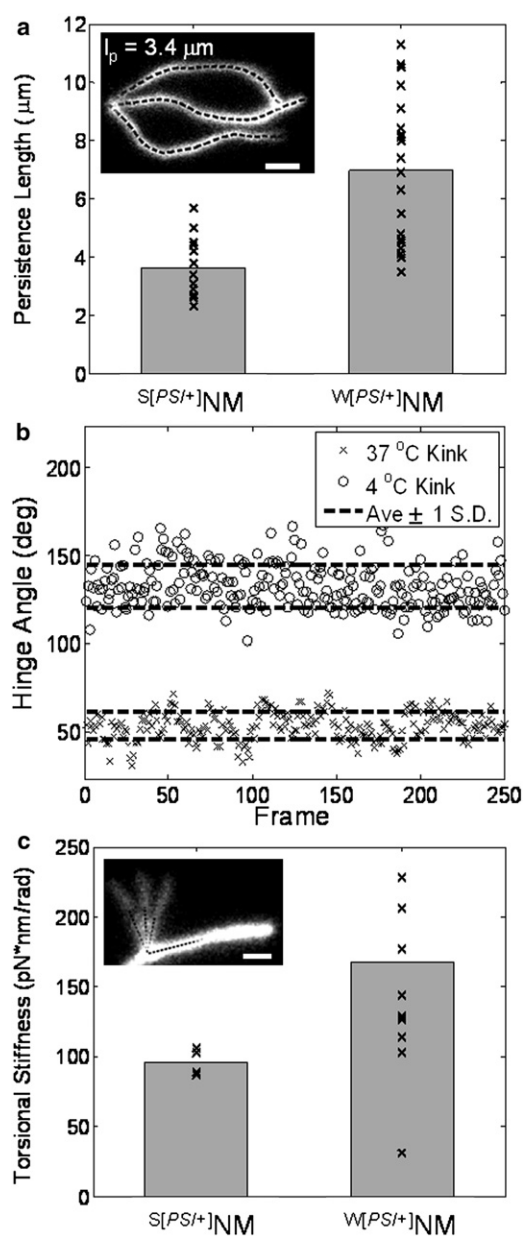
FIGURE 5 Fluorescence imaging was used to track the variations in shape of NM fibers subject to thermal fluctuations. (*a*) The persistence-length results of a bending mode analysis are shown for $^{S[PSI+]}$NM and $^{W[PSI+]}$NM fibers. (*Inset*) Three overlaid screenshots of a fluctuating fiber, with their corresponding skeletonized shapes (*dotted black lines*; scale bar, 2 μm). The average persistence lengths determined from the shape-fluctuation analysis were 3.6 μm and 7.0 μm for $^{S[PSI+]}$NM and $^{W[PSI+]}$NM fibers, respectively. (*b*) The fluctuations in kink angle of one $^{S[PSI+]}$NM and one $^{W[PSI+]}$NM kinked fiber are shown, along with the variance of each. (*c*) The variance was used to determine the kink torsional stiffness for $^{S[PSI+]}$NM and $^{W[PSI+]}$NM fibers, which shows a similar trend to the bending stiffness of homogeneous fibers.

thermal fluctuations of a $^{W[PSI+]}$NM kink. The torsional stiffness, κ_θ, is extracted from the angle θ using the equation

$$k_b T = \kappa_\theta \langle \theta^2 \rangle. \qquad (7)$$

$^{S[PSI+]}$NM fiber kinks ($N = 4$ measurements) exhibited an average torsional stiffness of 100 $\pm$ 10 pN·nm/rad, whereas the $^{W[PSI+]}$NM fiber kinks with no overlapping monomers were stiffer, with an average κ_θ of 170 $\pm$ 80 pN·nm/rad ($N = 3$). The $^{W[PSI+]}$NM fiber kinks with overlapping monomers gave a similar κ_θ of 210 $\pm$ 60 pN·nm/rad ($N = 3$), and the cross-linking kinks were also similar, with an average κ_θ of 170 $\pm$ 70 pN·nm/rad ($N = 6$). θ_0 varied over similar ranges for both $^{S[PSI+]}$NM fiber (59–131°) and $^{W[PSI+]}$NM fiber (54–115°) fibers.

DISCUSSION

Physical characterization of prion fibers has implications for prion biology and for the engineering and design of amyloid-based nanomaterials. In this work, we used two experimental methods, one active and one passive, to dynamically measure the physical properties of amyloid fibers in solution. Persistence lengths for other nonprion amyloid fibers have been measured previously under surface-bound conditions by shape analysis (i.e., tangent-angle correlations) (34,37) or atomic force microscopy (AFM) bending of surface-bound fibers suspended over grooves (34). As shown here by fluorescence imaging, the equilibrium morphologies of isolated NM fibers in solution often contain structural inhomogeneities, including local regions of static curvature and point inhomogeneities (i.e., kinks). Our analysis has demonstrated that fluorescence imaging is useful to identify potential structural inhomogeneities in fibers; and when structural inhomogeneities do exist, quantifying the fiber microstructure is necessary to properly characterize its physical properties. Furthermore, both of our approaches, bending-mode analysis by fluctuation imaging and force-extension measurement by optical trapping, have the advantage of making dynamic measurements on fibers in solution while simultaneously identifying fiber microstructure.

The persistence length of $^{S[PSI+]}$NM fibers was found to be 1.5 $\pm$ 0.6 μm from force-extension measurements (active measurement) and 3.6 $\pm$ 1.1 μm from thermal fluctuation analysis (passive measurement). In a similar way, the persistence length of $^{W[PSI+]}$NM fibers was found to be 3.3 $\pm$ 1.5 μm from force-extension and 7.0 $\pm$ 2.4 μm by thermal fluctuation analysis. Based on the shape analysis under surface-bound conditions, the persistence length of insulin fibrils, amyloid β peptide (Aβ), and a short peptide fragment of transthyretin were ~5–40 μm, ~100 μm, and ~300 μm, respectively (34,37). Even allowing for the uncertainties due to differences in technique, as discussed, it seems that NM fibrils are much less resistant to bending than these other amyloids. As previously shown for actin filaments, the reduced resistance to bending is indicative of greater susceptibility to fragmentation (38). This finding supports the emerging hypothesis that fragmentation efficiency is a key feature distinguishing prions from nonprion amyloids (17,39). The nonprion amyloids might be too rigid

to be fragmented by chaperones or other cellular factors and, therefore, have insufficient seeding capacity to function as protein-based elements of inheritance. Our results showed that [W[PSI+]]NM fibers had at least a twofold increase in bending stiffness (persistent length) compared to [S[PSI+]]NM fibers embodying the strong prion phenotype. These observations are also consistent with the hypothesis that more rigid amyloids are not fragmented effectively, generate seeds less efficiently, and result in weaker prion phenotypes in vivo (40). In addition, the tendency of [W[PSI+]]NM fibers to cross-link might result in networks in vivo, which would further impede fiber fragmentation.

Our combined force-fluorescence approach enabled active measurement of the extensional stiffness of NM fibers in addition to their L_p. In general, the modulus of nanoscale fibers as measured in extension can be different from that reduced from bending, since distinct molecular-level mechanisms may govern these different deformations. For example, Liu et al. found that elastic moduli of actin filaments obtained by extensional stiffness versus bending stiffness (35) differed by a factor of 3, and steered molecular dynamics simulations suggest that amyloid fiber structures may have distinct mechanical properties in extension versus in bending (41). Force-extension experiments on [S[PSI+]]NM fibers revealed a L_p of 1.5 μm and axial stiffness (K) of 5600 pN. Assuming a cylindrical geometry with a diameter of 4.5 nm (measured by AFM), we reduced elastic moduli of 0.26 GPa and 0.35 GPa from L_p (bending) and K (extension), respectively. These values represent a lower bound to the elastic modulus of NM fibers since the entire cross section may not experience mechanical load (42). The close agreement suggests that [S[PSI+]]NM indeed has a regular structure where the same molecular interactions and deformation mechanisms govern bending and axial mechanics of NM fibers. Recent results of Knowles et al. suggest that these molecular interactions are likely dominated by backbone β-sheet hydrogen bonds (37).

Elastic moduli can be similarly reduced from the persistence-length results of the shape-fluctuation experiments given the diameters measured by AFM (4.5 $\pm$ 0.7 nm and 5.2 $\pm$ 0.6 nm for the [S[PSI+]]NM and [W[PSI+]]NM fibers, respectively). This yields elastic moduli of 0.75 for [S[PSI+]]NM fibers and 0.80 GPa for [W[PSI+]]NM fibers. Again the material properties are in close agreement, suggesting that the physical behavior of polymorphic amyloid variants is also governed by similar molecular interactions, and that distinct physical properties are conferred by variations in folding geometry.

Fiber inhomogeneities resulted in either local regions of static curvature or sharp kinks. It is possible that kinks are locally unfolded regions creating flimsy domains where bending is easy. However, this is unlikely because the kink deformation energy ($\kappa_\theta \theta^* = 0.98 \times 10^{-19}$ N·m) is large compared to $k_B T$, and the torsional stiffness ($\kappa_\theta = 1.02 \times 10^{-19}$ N·m/rad) is even comparable to some actin

cross-linking proteins such as Arp2/3 ($\kappa_\theta = 0.8$–1.3×10^{-19} N·m/rad) (43). It is more likely that kinks form due to inhomogeneities in the folding configuration of monomers. Molecular dynamics simulations showed that a synthetic 8-mer peptide can assemble into amyloid fibers with kinks when monomers are able to adopt distinct folded geometries that have comparable thermodynamic stability (42). A significant fraction of [W[PSI+]]NM fibers had cross-links and kinks with overlapping monomers, whereas the [S[PSI+]]NM fiber contained none. Variation and differences in morphology can arise at different levels, suggesting distinct assembly pathways. At least two steps—nucleation, which is often a slow process, and elongation, a much more rapid process—are involved in amyloid formation. The morphological variation can arise at the level of nucleation, since various multiple-nucleation pathways have been reported for other amyloid proteins (44). The variation could also arise at the level of propagation. It has been observed that glucagon fibrils can continuously form new fibrils from existing fibrils by branching, whereas the fibril growth of Aβ (1–40) is linear (45). Different assembly conditions may promote different oligomeric species for nucleation, or favor different elongation mechanisms, thus giving rise to distinct morphologies. In any case, [W[PSI+]]NM assembly leaves fibers susceptible to interfiber cross-links along the length of the fiber and possibly at the ends, which may explain the increased adhesion of NM-coated beads along the side of the fiber.

Using force-fluorescence microscopy provides an accurate and thorough characterization of NM-fiber mechanical properties, which can facilitate the design and application of amyloid fibers as novel NMs. The obtained elastic modulus range, 0.35–0.80 GPa, places NM-fiber mechanical properties near those of spider silk (elastic modulus range 1–10 GPa (46)), making them an exceptionally stiff nanomaterial, with the ability to tune both fiber mechanical properties and larger-scale fiber network architecture (i.e., cross-linked versus entangled networks) via assembly conditions. Furthermore, NM fibers are remarkably stable. Neither [S[PSI+]]NM nor [W[PSI+]]NM fibers could be ruptured at forces up to 250 pN applied at quasistatic loading rates resulting in a minimum tensile strength of 0.05 GPa (assuming a cylindrical cross section and a diameter of 4.5 nm). Amyloid fibers also have distinct advantages compared to other nanomaterials. In particular, they can be easily synthesized from a wide range of proteins and are readily functionalized by genetic engineering (12,47), providing a means for interfacing with other biological, synthetic, or hybrid materials in applications such as biosensors or cell scaffolds (10). These attributes combined with their impressive mechanical properties make amyloid fibers an attractive option for many NM applications.

In summary, we have characterized the physical microstructure and mechanical properties of amyloid fibers formed from the widely studied amyloidogenic N-terminal

fragment of the yeast strain *Saccharomyces cerevisiae* protein Sup35. We report what to our knowledge are the first measurements of the extensional stiffness of amyloid fibers and of torsional stiffness of fiber kinks and cross-links. We have identified assembly temperature as a potential means of manipulating fiber physical properties, and we identified the physical consequence of amyloid fibers that are self-assembled from polymorphic misfolded proteins as pointing to a structural basis for the phenotypic diversity conferred from the prion protein. Our results give valuable insight into the molecular aggregation process and provide useful guidance and insights for design of amyloid-based NMs and prion-disease targets. The experimental methods we have developed are robust and can be adapted to study the structure-function relations of a wide variety of amyloid fibers and other biopolymers.

SUPPORTING MATERIAL

Four movies, and additional text with equations, three figures, and references, are available at http://www.biophysj.org/biophysj/supplemental/S0006-3495(11)00713-2.

REFERENCES

1. Koo, E. H., P. T. Lansbury, Jr., and J. W. Kelly. 1999. Amyloid diseases: abnormal protein aggregation in neurodegeneration. *Proc. Natl. Acad. Sci. USA.* 96:9989–9990.

2. True, H. L., and S. L. Lindquist. 2000. A yeast prion provides a mechanism for genetic variation and phenotypic diversity. *Nature.* 407:477–483.

3. True, H. L., I. Berlin, and S. L. Lindquist. 2004. Epigenetic regulation of translation reveals hidden genetic variation to produce complex traits. *Nature.* 431:184–187.

4. Tyedmers, J., M. L. Madariaga, and S. Lindquist. 2008. Prion switching in response to environmental stress. *PLoS Biol.* 6:e294.

5. Shorter, J., and S. Lindquist. 2005. Prions as adaptive conduits of memory and inheritance. *Nat. Rev. Genet.* 6:435–450.

6. Glover, J. R., A. S. Kowal, …, S. Lindquist. 1997. Self-seeded fibers formed by Sup35, the protein determinant of [PSI+], a heritable prion-like factor of S. cerevisiae. *Cell.* 89:811–819.

7. MacPhee, C. E., and C. M. Dobson. 2000. Formation of mixed fibrils demonstrates the generic nature and potential utility of amyloid nanostructures. *J. Am. Chem. Soc.* 122:12707–12713.

8. Dong, J., J. M. Canfield, …, D. G. Lynn. 2007. Engineering metal ion coordination to regulate amyloid fibril assembly and toxicity. *Proc. Natl. Acad. Sci. USA.* 104:13313–13318.

9. Cui, H. G., M. J. Webber, and S. I. Stupp. 2010. Self-assembly of peptide amphiphiles: from molecules to nanostructures to biomaterials. *Biopolymers.* 94:1–18.

10. Gras, S. L., A. K. Tickler, …, C. E. MacPhee. 2008. Functionalised amyloid fibrils for roles in cell adhesion. *Biomaterials.* 29:1553–1562.

11. Scheibel, T., R. Parthasarathy, …, S. L. Lindquist. 2003. Conducting nanowires built by controlled self-assembly of amyloid fibers and selective metal deposition. *Proc. Natl. Acad. Sci. USA.* 100:4527–4532.

12. Baxa, U., V. Speransky, …, R. B. Wickner. 2002. Mechanism of inactivation on prion conversion of the *Saccharomyces cerevisiae* Ure2 protein. *Proc. Natl. Acad. Sci. USA.* 99:5253–5260.

13. Knowles, T. P., T. W. Oppenheim, …, M. E. Welland. 2010. Nanostructured films from hierarchical self-assembly of amyloidogenic proteins. *Nat. Nanotechnol.* 5:204–207.

14. Zhang, S. 2003. Fabrication of novel biomaterials through molecular self-assembly. *Nat. Biotechnol.* 21:1171–1178.

15. Corrigan, A. M., C. Müller, and M. R. Krebs. 2006. The formation of nematic liquid crystal phases by hen lysozyme amyloid fibrils. *J. Am. Chem. Soc.* 128:14740–14741.

16. Krishnan, R., and S. L. Lindquist. 2005. Structural insights into a yeast prion illuminate nucleation and strain diversity. *Nature.* 435:765–772.

17. Tanaka, M., S. R. Collins, …, J. S. Weissman. 2006. The physical basis of how prion conformations determine strain phenotypes. *Nature.* 442:585–589.

18. MacKintosh, F. C., J. Käs, and P. A. Janmey. 1995. Elasticity of semiflexible biopolymer networks. *Phys. Rev. Lett.* 75:4425–4428.

19. Eaglestone, S. S., B. S. Cox, and M. F. Tuite. 1999. Translation termination efficiency can be regulated in *Saccharomyces cerevisiae* by environmental stress through a prion-mediated mechanism. *EMBO J.* 18:1974–1981.

20. Serio, T. R., A. G. Cashikar, …, S. L. Lindquist. 1999. Yeast prion [psi +] and its determinant, Sup35p. *Methods Enzymol.* 309:649–673.

21. Shewmaker, F., R. B. Wickner, and R. Tycko. 2006. Amyloid of the prion domain of Sup35p has an in-register parallel β-sheet structure. *Proc. Natl. Acad. Sci. USA.* 103:19754–19759.

22. Wang, M. D., H. Yin, …, S. M. Block. 1997. Stretching DNA with optical tweezers. *Biophys. J.* 72:1335–1346.

23. Baumann, C. G., S. B. Smith, …, C. Bustamante. 1997. Ionic effects on the elasticity of single DNA molecules. *Proc. Natl. Acad. Sci. USA.* 94:6185–6190.

24. Wen, J. D., M. Manosas, …, I. Tinoco, Jr. 2007. Force unfolding kinetics of RNA using optical tweezers. I. Effects of experimental variables on measured results. *Biophys. J.* 92:2996–3009.

25. Khalil, A. S., J. M. Ferrer, …, A. M. Belcher. 2007. Single M13 bacteriophage tethering and stretching. *Proc. Natl. Acad. Sci. USA.* 104:4892–4897.

26. Brau, R. R., P. B. Tarsa, …, M. J. Lang. 2006. Interlaced optical force-fluorescence measurements for single molecule biophysics. *Biophys. J.* 91:1069–1077.

27. Tarsa, P. B., R. R. Brau, …, M. J. Lang. 2007. Detecting force-induced molecular transitions with fluorescence resonant energy transfer. *Angew. Chem. Int. Ed. Engl.* 46:1999–2001.

28. Dong, J. J., C. E. Castro, …, S. Lindquist. 2010. Optical trapping with high forces reveals unexpected behaviors of prion fibrils. *Nat. Struct. Mol. Biol.* 17:1422–1430.

29. Lang, M. J., C. L. Asbury, …, S. M. Block. 2002. An automated two-dimensional force clamp for single molecule studies. *Biophys. J.* 83:491–501.

30. Gittes, F., B. Mickey, …, J. Howard. 1993. Flexural rigidity of microtubules and actin filaments measured from thermal fluctuations in shape. *J. Cell Biol.* 120:923–934.

31. Palmer, J. S., C. E. Castro, …, M. C. Boyce. 2009. Constitutive models for the force-extension behavior of biological filaments. *Proc. IUTAM Symp. Cell. Mol. Tissue Mech.* 141–159.

32. Marko, J. F., and E. D. Siggia. 1995. Stretching DNA. *Macromolecules.* 28:8759–8770.

33. Ott, A., M. Magnasco, …, A. Libchaber. 1993. Measurement of the persistence length of polymerized actin using fluorescence microscopy. *Phys. Rev. E.* 48:R1642–R1645.

34. Smith, J. F., T. P. J. Knowles, …, M. E. Welland. 2006. Characterization of the nanoscale properties of individual amyloid fibrils. *Proc. Natl. Acad. Sci. USA.* 103:15806–15811.

35. Liu, X. M., and G. H. Pollack. 2002. Mechanics of F-actin characterized with microfabricated cantilevers. *Biophys. J.* 83:2705–2715.

36. van Mameren, J., K. C. Vermeulen, …, C. F. Schmidt. 2009. Leveraging single protein polymers to measure flexural rigidity. *J. Phys. Chem. B.* 113:3837–3844.

37. Knowles, T. P., A. W. Fitzpatrick, …, M. E. Welland. 2007. Role of intermolecular forces in defining material properties of protein nanofibrils. *Science.* 318:1900–1903.

38. Goldmann, W. H. 2000. Binding of tropomyosin-troponin to actin increases filament bending stiffness. *Biochem. Biophys. Res. Commun.* 276:1225–1228.

39. Kushnirov, V. V., A. B. Vishnevskaya, …, M. D. Ter-Avanesyan. 2007. Prion and nonprion amyloids: a comparison inspired by the yeast Sup35 protein. *Prion.* 1:179–184.

40. Tanaka, M., P. Chien, …, J. S. Weissman. 2004. Conformational variations in an infectious protein determine prion strain differences. *Nature.* 428:323–328.

41. Keten, S., and M. J. Buehler. 2008. Large deformation and fracture mechanics of a β-helical protein nanotube: atomistic and continuum modeling. *Comput. Methods Appl. Mech. Eng.* 197:3203–3214.

42. Park, J., B. Kahng, …, W. Hwang. 2006. Atomistic simulation approach to a continuum description of self-assembled β-sheet filaments. *Biophys. J.* 90:2510–2524.

43. Blanchoin, L., K. J. Amann, …, T. D. Pollard. 2000. Direct observation of dendritic actin filament networks nucleated by Arp2/3 complex and WASP/Scar proteins. *Nature.* 404:1007–1011.

44. Serio, T. R., A. G. Cashikar, …, S. L. Lindquist. 2000. Nucleated conformational conversion and the replication of conformational information by a prion determinant. *Science.* 289:1317–1321.

45. Andersen, C. B., H. Yagi, …, C. Rischel. 2009. Branching in amyloid fibril growth. *Biophys. J.* 96:1529–1536.

46. Vollrath, F., and D. P. Knight. 2001. Liquid crystalline spinning of spider silk. *Nature.* 410:541–548.

47. Gras, S. L., A. M. Squires, …, C. E. MacPhee. 2006. Functionalised fibrils for bio-nanotechnology. *Int. Conf. Nanosci. Nanotech.* 29:1335–1346.